Atmos. Meas. Tech. Discuss., 6, 6975–7003, 2013
www.atmos-meas-tech-discuss.net/6/6975/2013/
doi:10.5194/amtd-6-6975-2013


Atmospheric Measurement Techniques Discussions



# Characterization of aura tropospheric emissions spectrometer carbonyl sulfide retrievals

**L. Kuai[1], J. Worden[2], S. S. Kulawik[2], S. A. Montzka[3], and J. Liu[1]**

[1]California Institute of Technology, Pasadena, California, USA
[2]Jet Propulsion Laboratory, California Institute of Technology, Pasadena, California, USA
[3]Global Monitoring Division, NOAA Earth System Research Laboratory, Boulder, Colorado, USA

Received: 5 July 2013 – Accepted: 16 July 2013 – Published: 31 July 2013

Correspondence to: L. Kuai (lkuai@jpl.nasa.gov) and J. Worden (john.r.worden@jpl.nasa.gov)

Published by Copernicus Publications on behalf of the European Geosciences Union.







## Abstract

We present a description of the Tropospheric Emission Spectrometer (TES) carbonyl sulfide (OCS) retrieval algorithm, along with evaluation of the biases and uncertainties against aircraft profiles from the HIPPO campaign and data from the NOAA Mauna Loa site. In general, the OCS retrievals (1) have less than 1.0 degree of freedom for signals (DOFs), (2) are sensitive in the mid-troposphere with a peak sensitivity typically between 300 to 500 hPa, (3) but have much smaller systematic errors from temperature, $CO_2$ and $H_2O$ calibrations relative to random errors from measurement noise. Here we estimate the monthly means from TES measurements averaged over multiple years so that random errors are reduced and useful information about OCS seasonal and latitudinal variability can be derived. With this averaging, TES OCS data are found to be consistent (within the calculated uncertainties) with NOAA ground observations and HIPPO aircraft measurements. TES OCS data also captures the seasonal and latitudinal variations observed by these in situ data.

## 1 Introduction

Carbonyl sulfide (OCS) significantly influences the sulfur cycle (Ko et al., 2003; Notholt et al., 2003, 2006; Montzka et al., 2007). It has a greenhouse gas effect based on absorption of far-infrared radiation (Brühl et al., 2012). OCS is also found as a potential trace gas, other than carbon dioxide, that could provide independent information about carbon cycle processes (Montzka et al., 2007; Campbell et al., 2008; Suntharalingam et al., 2008; Wohlfahrt et al., 2012; Blonquist et al., 2011; Berry et al., 2013). For example, recent work by Campbell et al. (2008) suggests that carbonyl sulfide is a good photosynthetic tracer. A study by Asaf et al. (2013) concludes that OCS flux could provide a constraint on estimates of gross primary productivity (GPP).

Carbonyl sulfide sources and sinks, however, are poorly quantified (Montzka et al., 2007). The major source of atmospheric carbonyl sulfide comes from the ocean (Cutter





AMTD
6, 6975–7003, 2013



et al., 2004), but other sources include wetlands, soil and precipitation, biomass burning, volcanoes, anthropogenic activities, and oxidation of carbon disulfide and dimethyl sulfide (Montzka et al., 2007; Watts, 2000). The primary sinks of carbonyl sulfide are vegetation, soil and photochemical loss (Montzka et al., 2007).

The mixing ratio of OCS is about 500 ppt (parts-per-trillion) and OCS is generally well mixed over the ocean and decreases rapidly with altitude in the stratosphere (Chin and Davis, 1995; Notholt et al., 2003; Barkley et al., 2008). However, latitudinal, seasonal, and longitudinal variations are about 10 % or even larger over land. Earlier studies have reported a slow decline in OCS mixing ratios in both hemispheres since the 1980s (Rinsland et al., 2002, 2008; Montzka et al., 2004; Mahieu et al., 2003). A recent study of one individual ground-based site, however, suggests no consistent trend during the period of February 2000–February 2005 (Montzka et al., 2007).

Atmospheric OCS concentrations in the free troposphere and boundary layer are currently measured at ground stations, tall towers, and aircraft using flask sampling or continuous measuring equipment. The NOAA-ESRL global monitoring network provides continuous records of OCS at 14 sampling sites (Montzka et al., 2007). The first satellite retrievals of carbonyl sulfide were based on solar occultation observations of the upper troposphere and stratosphere made by the Atmospheric Chemistry Experiment Fourier Transform Spectrometer (ACE-FTS) (Barkley et al., 2008). These observations during 2004–2006 provided an estimate of the stratospheric lifetime of OCS along with concurrent measurements of chlorofluoro-carbons (CFCs). In this paper, we evaluate free tropospheric OCS measurements from the Aura Tropospheric Emissions Spectrometer (TES) over ocean scenes. The Aura TES instrument is a high-resolution infrared-imaging Fourier transform spectrometer (Beer, 2006; Bowman et al., 2006). To evaluate the performance of algorithms, the TES free tropospheric OCS is compared with the independent NOAA observations from a ground-based site at Mauna Loa (MLO) (Montzka et al., 2007) and the measurements also made by the same NOAA laboratory during the HIAPER Pole-to-Pole Observations (HIPPO) flights (Wofsy et al., 2011).





AMTD
6, 6975–7003, 2013



## 2 Retrieval strategy

### 2.1 Retrieval methodology

The TES OCS retrieval is based on an optimal estimation (O.E.) approach (Rodgers, 2000) by fitting calculated spectra from a nonlinear radiative transfer model driven by the atmospheric state to the TES observed spectral radiances. The estimated state is also constrained by an a priori based on its probability distribution for that state in order to ensure a meaningful result (Bowman et al., 2006). The goal of this approach is to minimize the cost function, $\chi(\boldsymbol{x})$:

$$\chi(\boldsymbol{x}) = (\boldsymbol{y}_\mathrm{m} - \boldsymbol{y}_\mathrm{o})^\mathrm{T}\mathbf{S}_\mathrm{n}^{-1}(\boldsymbol{y}_\mathrm{m} - \boldsymbol{y}_\mathrm{o}) + \left(\hat{\boldsymbol{x}} - \boldsymbol{x}_\mathrm{a}\right)^\mathrm{T}\mathbf{S}_\mathrm{a}^{-1}\left(\hat{\boldsymbol{x}} - \boldsymbol{x}_\mathrm{a}\right) \quad (1)$$

where, $\hat{\boldsymbol{x}}$, $\boldsymbol{x}_\mathrm{a}$ and $\boldsymbol{x}$ are the retrieved, a priori, and the "true" state vectors respectively. They are expressed in natural logarithm of volume mixing ratio. $\boldsymbol{y}_\mathrm{m}$ and $\boldsymbol{y}_\mathrm{o}$ are model calculated and observed spectral radiance. $\mathbf{S}_\mathrm{n}^{-1}$ and $\mathbf{S}_\mathrm{a}^{-1}$ are inversion of the covariance matrix for measurement noise and a priori for the retrieved state vectors. If a minimum to the cost function is found then the estimated state vector can be related to the true state vector in the following manner (Rodgers, 2000):

$$\hat{\boldsymbol{x}} = \boldsymbol{x}_\mathrm{a} + \mathbf{A}(\boldsymbol{x} - \boldsymbol{x}_\mathrm{a}) + \mathbf{G}\boldsymbol{n} + \mathbf{G}\mathbf{K}_\mathrm{b}(\boldsymbol{b} - \boldsymbol{b}_\mathrm{a}) \quad (2)$$

where, $\boldsymbol{n}$ is a vector of measurement noise on the spectral radiances. $\boldsymbol{b}$ and $\boldsymbol{b}_\mathrm{a}$ represent the true state and a priori of the state for those parameters which also affect the model radiance. The sensitivities of the radiance to those parameters (Jacobians) are $\mathbf{K}_\mathrm{b} = \frac{\partial L}{\partial \boldsymbol{b}}$. It is the dependence of the radiance ($L$) on the interfering parameter ($\boldsymbol{b}$). $\mathbf{G}$ is the gain matrix, which is defined by

$$\mathbf{G} = \frac{\partial \boldsymbol{x}}{\partial L} = \left(\mathbf{K}^\mathrm{T}\mathbf{S}_\mathrm{n}^{-1}\mathbf{K} + \mathbf{S}_\mathrm{a}^{-1}\right)^{-1}\mathbf{K}^\mathrm{T}\mathbf{S}_\mathrm{n}^{-1} \quad (3)$$

$\mathbf{G}$ maps from measurement (spectral radiance) space into retrieval space. $\mathbf{A}$ is the averaging kernel matrix, which describes the sensitivity of the retrieval to the true state.





AMTD
6, 6975–7003, 2013



The trace of the averaging kernel gives the number of degrees of freedom for signals (DOFs) from the retrieval.

$$\mathbf{A} = \frac{\partial \hat{\boldsymbol{x}}}{\partial \boldsymbol{x}} = \mathbf{GK} \tag{4}$$

The carbonyl sulfide retrievals are carried out after the retrievals of temperature, water vapor, ozone, carbon monoxide, carbon dioxide, methane, surface temperature, emissivity, cloud optical depth, and cloud pressure (Kulawik et al., 2006). We only perform retrievals for scenes with cloud optical depth less than 0.5 as clouds reduce the sensitivity of observed radiance to atmospheric OCS. Adjustments to the atmospheric $CO_2$, $H_2O$, surface temperature, cloud optical depth, and cloud pressure are applied simultaneously with the OCS retrieval.

## 2.2 TES OCS spectral windows

Figure 1a shows the OCS absorption spectral region from 2034 to 2075 $cm^{-1}$. In order to show the impact of the OCS lines on the radiances, we compute simulated radiances using the geophysical parameters affecting the observed radiance (e.g. water vapor, $CO_2$, CO, ozone, surface temperature, cloud optical depth, cloud pressure, and emissivity) and the OCS profile. Then we repeat the calculations with the same atmosphere but without OCS (Fig. 1a). The residuals of the two radiances are shown in Fig. 1b, which illustrates the absorption by OCS. It is also the OCS column Jacobians. The contour plot of OCS Jacobians (Fig. 1c) suggests that the radiances are more sensitive to OCS between 900 to 200 hPa. For comparison to the noise level, the Noise Equivalent Spectral Radiance (NESR) in this region is $1 \times 10^{-8}$ $W\,cm^{-2}\,sr^{-1}\,cm^{-1}$ indicating that the OCS signal to noise ratio in this region is approximately one for each of the strong absorption lines.

Figure 1d shows the column Jacobians of the absorption gases in addition to OCS at this spectral region. Water vapor (blue line) and $CO_2$ (green line) are dominant in this spectral region. CO and ozone are active on some spectral lines. For these





AMTD
6, 6975–7003, 2013



reasons, $CO_2$ and $H_2O$ are simultaneously estimated with OCS but are constrained using estimates from a previous retrieval using different spectral bands measured by TES (Kulawik et al., 2010; Worden et al., 2004). CO concentrations are not jointly retrieved with OCS but have been determined from a CO estimate using the CO band near 2100 $cm^{-1}$ (Worden et al., 2004).

### 2.3 A priori vectors and constraints

In addition to OCS, we also simultaneously retrieve surface temperature, $H_2O$, $CO_2$, cloud optical depth, and cloud pressure level. If over land, emissivity is also required to be retrieved for that spectral region. In this paper, we only report the retrievals over ocean. We do not take into account the impact of aerosols on OCS retrievals since the spectral region we use are from the mid-infrared region and aerosols from biomass burning negligibly affect the retrievals (Shephard et al., 2011; Verma et al., 2009; Worden et al., 2013). Although significant dust from the desert could affect mid-IR retrievals, the current study is limited to over the Pacific and aerosols there are mostly from biomass burning.

The a priori profile of OCS is set to a constant value of 500 ppt in the free troposphere and decreases with altitude above the tropopause (Fig. 2). No obvious long-term trend is observed in atmospheric OCS, so at this stage we simply use a common OCS a priori profile to ensure that the retrieved spatiotemporal variations are not coming from the a priori.

Typically for an O.E. retrieval, the covariance $\mathbf{S}_a$ term describes the expected statistics of the retrieved parameter and also acts to constrain the values that are allowed for the estimate. However, we relax this term for the OCS retrievals in order to increase sensitivity of the estimated OCS to true OCS variations at the expense of increasing errors from random noise or interferences (Worden et al., 2010). This approach works for OCS because, as demonstrated in Sect. 3.2, the uncertainties are dominated by noise. Errors from interferences such as temperature and $H_2O$, which can alia into the observed variability of the OCS estimates, are found to be much smaller than the noise





AMTD
6, 6975–7003, 2013



based error. Consequently, we can average the OCS estimates as the uncertainties are effectively random.

The top panels in Fig. 3 show the square roots of the diagonals of the covariance matrices. The dots on the profile indicate the retrieval levels. Note that the covariance matrices are calculated in natural logarithm; consequently, the values are in percentage. The covariance matrices are plotted on the bottom of Fig. 3. Inverting these covariance matrices generates the constraint matrices.

## 3 TES carbonyl sulfide product

### 3.1 TES OCS detection limits and retrieval characteristics

Figure 4 shows comparisons of TES radiances near Mauna Loa with modeled radiances that depend on the set of geophysical parameters affecting the observed radiance. We choose three examples of TES observations near Mauna Loa. "$d1$" (light blue in Fig. 4a, c, e) is the difference between measured TES spectra and forward model runs with retrieved variables but no OCS. "$d2$" (red in Fig. 4a, c, e) is the difference between two forward-model runs with and without OCS or column jacobians of OCS. The spikes in $d1$ are related to the OCS absorption in $d2$, which suggests that without the simulation of the absorption by OCS, the residuals $d1$ still contain the information of OCS ($d2$). Then, we show the residuals after we retrieve OCS ($d3$, light blue with dots in Fig. 4b, d, f). The spikes related to OCS absorption are no longer shown in $d3$. Dots on $d3$ indicate the frequency of the channels selected for the retrievals.

The first example in Fig. 4a and b represents an atmosphere with low OCS concentration so the OCS signal ($d1$ in red line) is weak, about or even below the noise level (dashed lines). The second and third examples (Fig. 4c–f) show strong OCS signals. If OCS is not retrieved with these radiances, the residuals ($d1$) are biased below zero, especially at the region with strong OCS absorption lines near 2050 $\mathrm{cm}^{-1}$ and





AMTD
6, 6975–7003, 2013



2070 $cm^{-1}$. With the OCS retrieval, however, the residuals ($d3$) are much more random and symmetric about zero.

Due to the low sensitivity of the TES observed radiances to OCS relative to $H_2O$ and $CO_2$, the TES spectrum gives limited information about the OCS profile. In general, under clear-sky conditions, TES estimates are sensitive to the OCS distribution from 900 to 200 hPa with a peaked sensitivity near 400 hPa. The sensitivity of the OCS estimate is primarily determined by the surface temperature and thermal contrast between surface and atmospheric temperature. Figure 5a shows the averaging kernels at different vertical levels for a single sounding retrieval. The black line is one tenth of the column-averaging kernel. If the column-averaging kernel is close to one, the retrieved state will vary exactly the same as the true state (in the absence of errors). The DOFs for this retrieval are 0.67. The retrieved OCS profile is plotted in Fig. 5b as black line with dots. Since in the free troposphere, OCS is quite well mixed and the analysis of averaging kernel suggests that TES OCS estimates are most sensitive to a vertical range centered near 400 hPa, with less than 1 DOFs, we use the average of the retrieved OCS between 900 to 200 hPa to represent the TES retrieved tropospheric OCS (red in Fig. 5b).

### 3.2 Retrieval error analysis

Figure 6 shows the reduction of the uncertainties after the TES retrieval by comparing the a posteriori uncertainties (or total error, dashed line) to the a priori uncertainties (black line with dots). The total error for an individual retrieval, however, is still quite large at about 50 to 80 ppt, almost of the same order of magnitude of the OCS seasonal variations in the Northern Hemisphere. Fortunately, the dominant errors come from measurement noise as random errors. The primary three systematic errors due to $CO_2$, $H_2O$ and temperature are much smaller (< 5 ppt) than the measurement error, so we plot the ten times of their original values in Fig. 6. The error analysis suggests that by





AMTD
6, 6975–7003, 2013



averaging a large number of retrievals, for example averaging the monthly data over multiple years, the total error can be greatly reduced.

To evaluate the TES OCS estimates, we compare its multiple-year monthly average with independent and more accurate observations. The quality of monthly TES estimated tropospheric OCS averaged over several years and inside a large grid box centered with in situ observations is evaluated in Sect. 3.3.

### 3.3 Assessment of the quality of the TES product and the bias correction

To evaluate the performance of the TES OCS retrieval we perform a comparison of monthly means over multiple years between the in situ data and the TES retrieved estimates for seasonal variability over Mauna Loa and for latitudinal gradient over the Pacific region. As shown in the previous section systematic errors from radiative interferences such as $H_2O$, $CO_2$, and temperature are small i.e. less than 5 ppt. Measurement noise is the largest uncertainty of the OCS estimates (not including "smoothing" error). This measurement noise is random and consequently the OCS estimates can be averaged with a reduction of error corresponding to the square root of the number of the observations. With averaging over multiple years we gain sensitivity to seasonal and latitudinal variations with the TES data.

By applying the TES averaging kernel, **A**, and a priori, $\chi_a$, to the in situ observed concentration profile ($\chi_{std}^{OCS}$), we can perform the comparison between the TES tropospheric OCS and vertically convolved observations that accounts for the a priori regularization together with the sensitivity and vertical resolution of the TES retrievals:

$$\ln\left(\chi_{std\_AK}^{OCS}\right) = \ln(\chi_a) + \mathbf{A}\left(\ln\left(\chi_{std}^{OCS}\right) - \ln(\chi_a)\right) \quad (5)$$

By comparing to both HIPPO aircraft results and Mauna Loa ground-based measurements (obtained at 3.4 km a.s.l.), the TES overestimates the OCS by about 13 %. We attribute this result from the uncertainties in the spectroscopic line strengths. The correction for this bias must therefore account for the sensitivity of the retrieval. For





AMTD
6, 6975–7003, 2013



example, if the TES OCS estimate shows zero sensitivity, the estimate will return to the a priori constraint regardless of the spectroscopic uncertainties. For this reason we use the following form to estimate the bias correction by fitting the resulting observed OCS ($\chi^{\mathrm{OCS}}_{\mathrm{corrected}}$) with TES OCS, as discussed in Worden et al. (2006):

$$\ln\left(\chi^{\mathrm{OCS}}_{\mathrm{corrected}}\right) = \ln\left(\chi^{\mathrm{OCS}}_{\mathrm{std\_AK}}\right) + \mathbf{A}\left(\delta_{\mathrm{bias}}\right) \quad (6)$$

where $\chi^{\mathrm{OCS}}_{\mathrm{std\_AK}}$ is the standard volume mixing ratio from the ground-based or flight observations already convolved with TES averaging kernel using Eq. (5). **A** is the TES OCS averaging kernel matrix. The bias correction factor ($\delta_{\mathrm{bias}}$) is estimated to be 0.52 by comparing between HIPPO and TES data as discussed next. In this paper, the in situ data has to be applied with Eqs. (5) and (6), as referred to the TES operator, so that the bias corrected in situ data ($\chi^{\mathrm{OCS}}_{\mathrm{corrected}}$) can be compared with TES OCS estimates.

### 3.3.1 Latitudinal gradient over Pacific

The multi-year TES OCS monthly means are compared to the measurements from five discrete HIPPO aircraft campaigns to study the latitudinal patterns during different seasons across the Pacific Ocean. We only used the HIPPO OCS measurements by NWAS-M2 (NOAA Whole Air Sampler–Mass Spectrometer #2), one of their three instruments ("OCS_M2" data from "HIPPO NOAA Flask Sample GHG, Halocarbon, And Hydrocarbon Data" in file "HIPPO_noaa_flask_allparams_merge_insitu_20121129.tbl"; this data file could be downloaded at website: http://hippo.ornl.gov/dataaccess) (Wofsy et al., 2011).

Our approach of comparison to HIPPO data is to average several years of TES data corresponding in latitude, longitude and month. This approach assumes that OCS atmospheric concentrations do not vary significantly within the spatial and temporal bins. In addition HIPPO tropospheric data is first averaged vertically and within each latitude and longitude bin in order to reduce the variability of short term mixing processes.





AMTD
6, 6975–7003, 2013



This averaged concentration is then remapped back to the TES pressure grid in the troposphere, before application of Eqs. (5) and (6).

The HIPPO trajectories are plotted in Fig. 7 (dots). The gray regions are the overpassing TES data closest to the HIPPO flights. The HIPPO profiles are vertically averaged between 900 hPa and 200 hPa and latitudinal averaged onto regular grids from 35° S to 35° N every 10° (black dots in Fig. 8a–f). The original HIPPO latitudinal grid-binned data have been convolved with the TES averaging kernels and the bias corrections; see Eqs. (5) and (6). The resulted HIPPO latitudinal gradients are shown in Fig. 8a–f in blue lines with dots.

The measurements during each HIPPO campaign are collected within about 15 days during different months since 2009 to 2011 (see Table 1). The matching TES estimates are located within the grid box of ±10° about each HIPPO data and observed from space during the ±15 days time period of multiple years (2006 to 2010). These retrievals exclude observations over land, total SNR less than 40, cloud optical depth greater than 0.5 and retrieved chi square outside the range of 0.8 to 1.2. With these quality flags, we generally exclude higher-latitude regions. The retrievals are also binned into the same regular latitudinal grids from 35° S to 35° N every 10° (Fig. 8a–f red dots). Errors on the mean are shown as error bars, which range from 4 to 7 ppt.

The multi-year monthly-averaged TES retrievals and results from the five HIPPO measurements applied with TES operator in general exhibit similar latitudinal variations with fairly good correlation coefficients ($R > 0.6$). Although small differences remain in each comparison, the standard deviation (SD) of their differences is consistent with the magnitude of the calculated mean errors.

### 3.3.2 Seasonal variations over Mauna Loa

We also perform a comparison of the TES multi-year monthly average within a grid box of 10° by 10° latitude/longitude centered at Mauna Loa (19.5° N, 155.6° W) to the ground station measurements at Mauna Loa site (MLO), a high-altitude site within a global air-sampling network (Montzka et al., 2007). The measurements of OCS





AMTD
6, 6975–7003, 2013



from flasks filled with ambient air at the Mauna Loa Observatory at ~ 3.4 km a.s.l. from a tower 40 m a.g.l. on the side of the Mauna Loa volcano. The replicate measurement precision for OCS from flasks is typically less than 1 %. Flask samples are collected in mid-morning and typically represent free tropospheric air. The magnitude of the observed seasonal variation at this high-altitude surface site is about 9 % (or 44 ppt). This variation and that derived from other NOAA flasks measurements regularly made in the free troposphere (above 2 km a.s.l.) is relatively small compared to the seasonal variation observed at low-altitude continental sites in higher latitudes of the Northern Hemisphere (Montzka et al., 2007).

In Fig. 8g, we show OCS results by averaging the TES retrievals with at least 0.5 DOFs over Mauna Loa within a grid box of 10° by 10° by monthly average over 2006 to 2010 (red dots). The same quality flag described in HIPPO comparison is applied. The NOAA Mauna Loa monthly averages over the same period, from 2006 to 2010, at the surface site are plotted in black dots in Fig. 8g. The blue line is the MLO monthly averages after applying the TES operator. The comparison between red and blue suggests that with the TES limited sensitivity, e.g. the DOFs for OCS are between 0.5 and 1, only about 20 ppt of the seasonal variation can be observed from space. TES retrieved monthly mean (red dots), however, varies consistently with the corresponding ground-based monthly mean. The error bar shows the error on the mean of TES monthly values determined in multiple years. On average, the uncertainty of these TES monthly means is about 7 ppt and standard deviation (SD) of the differences is about 5 ppt. There is about −15 ppt bias, larger than the bias in HIPPO-TES comparisons, as expected because MLO data only measures the OCS concentration near the surface at 3.4 km.

### 3.3.3 Comparison to all HIPPO data

Figure 9 shows the correlation of TES monthly OCS to corresponding all HIPPO estimates convolved with the TES operator. TES OCS shows fairly well correlation ($R$ = 0.66) with these bias corrected in situ data, which were applied with the TES





AMTD
6, 6975–7003, 2013



operator during different months of the year. The bias has been removed using the TES operator and the calculated TES overall SD error is about 7.74 ppt. The estimated precision of these averaged TES OCS estimates is about 5 ppt (the average of the total errors from single soundings divided by square root of the number of observations). The remaining difference between the calculated SD error and TES precision can be explained by (1) the averaging of TES data over several years whereas the OCS is expected to have some inter-annual variability, for example due to El Nino Southern Oscillation (ENSO); (2) additional variance because the retrieval problem is non-linear or (3) because of bias or smoothing errors from the co-retrieved $CO_2$ and $H_2O$ estimates (Fig. 6). Based on this comparison we would expect the accuracy of the TES OCS retrievals to have an upper bound of 5 ppt (not including the bias likely due to spectroscopy) in order to explain the remaining difference between the precision and the overall SD error to HIPPO data.

The calculated error is well explained by the expected error and is less than the magnitude of the observed seasonal variation and latitudinal gradient from the aircraft and surface data. The maximum-minimum differences for both latitudinal and seasonal variations are in general more than 10 ppt. Therefore, with the current precision, TES multi-year monthly OCS is capable to detect both latitudinal and seasonal variations. Table 1 summarizes comparisons for each data set by listing correlation coefficient ($R$), bias, SD error and TES precision. The Mauna Loa TES data has larger error bars than HIPPLO-matching TES data simply because its sample size is much smaller than the number of TES data for corresponding HIPPO measurements.

A Taylor diagram in Fig. 10 shows the performances of TES observed spatiotemporal pattern and variability compared to the processed in situ observations for different comparisons. The radius of the diagram is in the units of the standard deviation of the patterns observed from in situ data and the angle indicates the correlation to the in situ data. The perfect agreement with in situ observations is always located at one standard deviation and correlation of 1 (purple dot). The distance to the purple dot indicates the error. Individual comparison between TES and in situ data as in Fig. 8 are plotted in





AMTD
6, 6975–7003, 2013



red dots and the comparisons of TES to all HIPPOs are in green dot. In general, correlations are at least more than 0.6 and TES always observes larger variability than in situ observations.

## 4 Conclusions

In this paper we describe an approach to retrieve atmospheric carbonyl sulfide from TES spectra over the ocean and evaluate the results against in situ data. The algorithm is performed after retrievals of atmospheric temperature, surface temperature, water vapor, ozone, CO, $CO_2$, cloud optical depth and pressure level, and emissivity using co-measured radiances at other wavelengths. The retrieved results are obtained by fitting the OCS absorption band ranging from 2034 to 2075 $cm^{-1}$. Simultaneous retrieval of interfering species including water vapor and $CO_2$, based on the previous retrieved values, minimizes the impact of the systematic errors.

We carry out an initial assessment of the TES retrieval performance over ocean regions by comparing TES multi-year monthly average at Mauna Loa with the corresponding ground-based observations (MLO). We also compared the multi-year monthly mean TES data across the Pacific between 35° S to 35° N with measurements made during the five HIPPO campaigns across this region.

The retrievals have maximum sensitivity between 300 and 500 hPa but with DOFs that are typically less than 1.0. Typical uncertainties for a single observation, averaged over the troposphere, is 50 ppt. However, the uncertainties are primarily driven by noise in the TES spectra and consequently, these observations can be averaged to reduce the error. The TES data are biased high by about 13 %, but when averaged over multiple years and after accounting for the TES OCS sensitivities and noise, these data can capture the seasonal and latitudinal variability of tropospheric OCS. A future algorithm will examine the variability of quantifying OCS over land; this algorithm will include an estimate of surface emissivity, which can vary strongly enough to influence the OCS





AMTD
6, 6975–7003, 2013



retrieval. Care must therefore be taken to identify regions where emissivity variations are small enough to allow for an accurate estimate of OCS.

*Acknowledgements.* This work was carried out at the Jet Propulsion Laboratory, California Institute of Technology, under a contract with the National Aeronautics and Space Administration. We would also acknowledge Steve Wofsy, Elliot Atlas, Benjamin R. Miller, Fred Moore, James Elkins, and all other HIPPO team members (the pilots, mechanics, technicians, and scientific crew) for making the HIPPO data available. HIPPO was supported by NSF grants ATM – 0628575, ATM – 0628519, ATM – 0628388, and by the National Center for Atmospheric Research (NCAR). NCAR is supported by the NSF. The authors also wish to thank Yuk Yung, Elliott Campbell, Joe Berry, and Ian Baker for the helpful discussion.

## References

Asaf, D., Rotenberg, E., Tatarinov, F., Dicken, U., Montzka, S. A., and Yakir, D.: Ecosystem photosynthesis inferred from measurements of carbonyl sulphide flux, Nat. Geosci., 6, 186–190, doi:10.1038/ngeo1730, 2013.

Barkley, M. P., Palmer, P. I., Boone, C. D., Bernath, P. F., and Suntharalingam, P.: Global distributions of carbonyl sulfide in the upper troposphere and stratosphere, Geophys. Res. Lett., 35, L14810, doi:10.1029/2008gl034270, 2008.

Beer, R.: TES on the Aura Mission: scientific objectives, measurements, and analysis overview, IEEE T. Geosci. Remote, 44, 1102–1105, doi:10.1109/TGRS.2005.863716, 2006.

Berry, J., Wolf, A., Campbell, J. E., Baker, I., Blake, N., Blake, D., Denning, A. S., Kawa, S. R., Montzka, S. A., Seibt, U., Stimler, K., Yakir, D., and Zhu, Z.: A coupled model of the global cycles of carbonyl sulfide and $CO_2$: a possible new window on the carbon cycle, J. Geophys. Res.-Biogeo., 118, 1–11, doi:10.1002/jgrg.20068, 2013.

Blonquist, J. M., Montzka, S. A., Munger, J. W., Yakir, D., Desai, A. R., Dragoni, D., Griffis, T. J., Monson, R. K., Scott, R. L., and Bowling, D. R.: The potential of carbonyl sulfide as a proxy for gross primary production at flux tower sites, J. Geophys. Res., 116, G04019, doi:10.1029/2011jg001723, 2011.

Bowman, K. W., Rodgers, C. D., Kulawik, S., Worden, J., Sarkissian, E., Osterman, G., Steck, T., Lou, M., Eldering, A., Shephard, M., Worder, H., Lampel, M., Clough, S.,





AMTD
6, 6975–7003, 2013



Brown, P., Rinsland, C., Gunson, M., and Beer, R.: Tropospheric emission spectrometer: retrieval method and error analysis, IEEE T. Geosci. Remote, 44, 1297–1307, doi:10.1109/TGRS.2006.871234, 2006.

Brühl, C., Lelieveld, J., Crutzen, P. J., and Tost, H.: The role of carbonyl sulphide as a source of stratospheric sulphate aerosol and its impact on climate, Atmos. Chem. Phys., 12, 1239–1253, doi:10.5194/acp-12-1239-2012, 2012.

Campbell, J. E., Carmichael, G. R., Chai, T., Mena-Carrasco, M., Tang, Y., Blake, D. R., Blake, N. J., Vay, S. A., Collatz, G. J., Baker, I., Berry, J. A., Montzka, S. A., Sweeney, C., Schnoor, J. L., and Stanier, C. O.: Photosynthetic control of atmospheric carbonyl sulfide during the growing season, Science, 322, 1085–1088, doi:10.1126/science.1164015, 2008.

Chin, M. and Davis, D. D.: A reanalysis of carbon sulfide as a source of stratosphere background sulfer aerosol, J. Geophys. Res., 100, 8993–9005, 1995.

Cutter, G. A., Cutter, L. S., and Filippino, K. C.: Sources and cycling of carbonyl sulfide in the Sargasso Sea, Limnol. Oceanogr., 49, 555–565, 2004.

Ko, M. K. W., Poulet, G., Blake, D. R., Boucher, O., Burkholder, J. H., Chin, M., Cox, R. A., George, C., Graf, H.-F., Holton, J. R., Jacob, D. J., Law, K. S., Lawrence, M. G., Midgley, P. M., Seakins, P. W., Shallcross, D. E., Strahan, S. E., Wuebbles, D. J., and Yokouchi, Y.: Very Short-Lived Halogen and Sulfur Substances, Scientific Assessment of Ozone Depletion, Global Ozone Research and Monitoring Project – Report No. 47, World Meteorological Organization, Geneva, 2003.

Kulawik, S. S., Worden, H., Osterman, G., Luo, M., Beer, R., Kinnison, D. E., Bowman, K. W., Worden, J., Eldering, A., Lampel, M., Steck, T., and Rodger, C. D.: TES atmospheric profile retrieval characterization: an orbit of simulated observations, IEEE T. Geosci. Remote, 44, 1324–1333, doi:10.1109/TGRS.2006.871207, 2006.

Kulawik, S. S., Jones, D. B. A., Nassar, R., Irion, F. W., Worden, J. R., Bowman, K. W., Machida, T., Matsueda, H., Sawa, Y., Biraud, S. C., Fischer, M. L., and Jacobson, A. R.: Characterization of Tropospheric Emission Spectrometer (TES) $CO_2$ for carbon cycle science, Atmos. Chem. Phys., 10, 5601–5623, doi:10.5194/acp-10-5601-2010, 2010.

Mahieu, E., Rinsland, C. P., Zander, R., Duchatelet, P., and Servais, C.: Tropospheric and stratospheric carbonyl sulfide (OCS): long-term trends and seasonal cycles above the Jungfraujoch station, in The Sixth European Symposium on Stratospheric Ozone, 2–6 September, Goteborg, Sweden, 309–312, 2003.





AMTD
6, 6975–7003, 2013



Montzka, S. A., Aydin, M., Battle, M., Butler, J. H., Saltzman, E. S., Hall, B. D., Clarke, A. D., Mondeel, D. J., and Elkins, J. W.: A 350-year atmospheric history for carbonyl sulfide inferred from Antarctic firn air and air trapped in ice, J. Geophys. Res., 109, D22302, doi:10.1029/2004jd004686, 2004.

Montzka, S. A., Calvert, P., Hall, B. D., Elkins, J. W., Conway, T. J., Tans, P. P., and Sweeney, C.: On the global distribution, seasonality, and budget of atmospheric carbonyl sulfide (COS) and some similarities to $CO_2$, J. Geophys. Res., 112, D09302, doi:10.1029/2006jd007665, 2007.

Notholt, J., Kuang, Z., Rinsland, C. P., Toon, G. C., Rex, M., Jones, N., Albrecht, T., Deckelmann, H., Krieg, J., Weinzierl, C., Bingemer, H., Weller, R., and Schrems, O.: Enhanced upper tropical tropospheric COS: impact on the stratospheric aerosol layer, Science, 300, 307–310, doi:10.1126/science.1080320, 2003.

Notholt, J., Bingemer, H., Berresheim, H., Holton, J. R., Kettle, A. J., Mahieu, E., and Montzka, S.: Precursor Gas Measurement, SPARC Assessment of Stratospheric Aerosol Properties, SPARC Scientific Steering Group, Zurich, 2006.

Rinsland, C. P., Goldman, A., Mahieu, E., Zander, R., Notholt, J., Jones, N. B., Griffith, D. W. T., Stephen, T. M., and Chiou, L. S.: Ground-based infrared spectroscopic measurements of carbonyl sulfide: free tropospheric trends from a 24-year time series of solar absorption measurements, J. Geophys. Res., 107, 4657, doi:10.1029/2002jd002522, 2002.

Rinsland, C. P., Chiou, L., Mahieu, E., Zander, R., Boone, C. D., and Bernath, P. F.: Measurements of long-term changes in atmospheric OCS (carbonyl sulfide) from infrared solar observations, J. Quant. Spectrosc. Ra., 109, 2679–2686, doi:10.1016/j.jqsrt.2008.07.008, 2008.

Rodgers, C. D.: Inverse Methods for Atmospheric Sounding: Theory and Practice, World Scientific, London, 256 pp., 2000.

Shephard, M. W., Cady-Pereira, K. E., Luo, M., Henze, D. K., Pinder, R. W., Walker, J. T., Rinsland, C. P., Bash, J. O., Zhu, L., Payne, V. H., and Clarisse, L.: TES ammonia retrieval strategy and global observations of the spatial and seasonal variability of ammonia, Atmos. Chem. Phys., 11, 10743–10763, doi:10.5194/acp-11-10743-2011, 2011.

Suntharalingam, P., Kettle, A. J., Montzka, S. M., and Jacob, D. J.: Global 3-D model analysis of the seasonal cycle of atmospheric carbonyl sulfide: implications for terrestrial vegetation uptake, Geophys. Res. Lett., 35, L19801, doi:10.1029/2008gl034332, 2008.





AMTD
6, 6975–7003, 2013



Verma, S., Worden, J., Pierce, B., Jones, D. B. A., Al-Saadi, J., Boersma, F., Bowman, K., Eldering, A., Fisher, B., Jourdain, L., Kulawik, S., and Worden, H.: Ozone production in boreal fire smoke plumes using observations from the Tropospheric Emission Spectrometer and the Ozone Monitoring Instrument, J. Geophys. Res.-Atmos., 114, D02303, doi:10.1029/2008JD010108, 2009.

Watts, S. F.: The mass budgets of carbonyl sulfide, dimethyl sulfide, carbon disulfide and hydrogen sulfide, Atmos. Environ., 34, 761–799, 2000.

Wofsy, S. C., Team, H. S., Cooperating, M., and Satellite, T.: HIAPER Pole-to-Pole Observations (HIPPO): fine-grained, global-scale measurements of climatically important atmospheric gases and aerosols, Phil. Trans. R. Soc. A, 369, 2073–2086, doi:10.1098/rsta.2010.0313, 2011.

Wohlfahrt, G., Brilli, F., Hortnagl, L., Xu, X., Bingemer, H., Hansel, A., and Loreto, F.: Carbonyl sulfide (COS) as a tracer for canopy photosynthesis, transpiration and stomatal conductance: potential and limitations, Plant Cell Environ., 35, 657–667, doi:10.1111/j.1365-3040.2011.02451.x, 2012.

Worden, H. M., Deeter, M. N., Edwards, D. P., Gille, J. C., Drummond, J. R., and Nédélec, P.: Observations of near-surface carbon monoxide from space using MOPITT multispectral retrievals, J. Geophys. Res., 115, D18314, doi:10.1029/2010jd014242, 2010.

Worden, J., Kulawik, S. S., Shephard, M., Clough, S. A., Worden, H., Bowman, K., and Goldman, A.: Predicted errors of tropospheric emission spectrometer nadir retrievals from spectral window selection, J. Geophys. Res., 109, D09308, doi:10.1029/2004jd004522, 2004.

Worden, J., Bowman, K., Noone, D., Beer, R., Clough, S., Eldering, A., Fisher, B., Goldman, A., Gunson, M., Herman, R., Kulawik, S. S., Lampel, M., Luo, M., Osterman, G., Rinsland, C., Rodgers, C., Sander, S., Shephard, M., and Worden, H.: Tropospheric Emission Spectrometer observations of the tropospheric HDO/$H_2O$ ratio: estimation approach and characterization, J. Geophys. Res., 111, D09308, doi:10.1029/2005jd006606, 2006.

Worden, J., Wecht, K., Frankenberg, C., Alvarado, M., Bowman, K., Kort, E., Kulawik, S., Lee, M., Payne, V., and Worden, H.: $CH_4$ and CO distributions over tropical fires during October 2006 as observed by the Aura TES satellite instrument and modeled by GEOS-Chem, Atmos. Chem. Phys., 13, 3679–3692, doi:10.5194/acp-13-3679-2013, 2013.





AMTD
6, 6975–7003, 2013



**Table 1.** Lists of HIPPO measurement period, correlation coefficient, bias, SD, TES precision and sample number for the comparisons between TES multi-year monthly data and in situ data.

| In situ | HIPPO1 | HIPPO2 | HIPPO3 | HIPPO4 | HIPPO5 | MLO | All HIPPO |
|---|---|---|---|---|---|---|---|
| Year | 2009 | 2009 | 2010 | 2011 | 2011 | 2006–2010 | |
| First day | 14 Jan | 4 Nov | 29 Mar | 22 Jun | 22 Aug | 1 Jan | |
| Last day | 26 Jan | 19 Nov | 13 Apr | 07 Jul | 06 Sep | 31 Dec | |
| *R* | 0.93 | 0.80 | 0.71 | 0.90 | 0.61 | 0.82 | 0.66 |
| Bias (ppt) | 2.34 | 7.63 | 0.22 | −2.30 | −5.55 | −14.91 | 0.06 |
| SD (ppt) | 8.14 | 7.49 | 6.35 | 8.01 | 5.12 | 4.69 | 7.74 |
| TES precision (ppt) | 4.45 | 4.50 | 4.71 | 4.55 | 3.84 | 7.30 | |
| TES sample number | 208–716 | 153–505 | 139–447 | 293–428 | 190–566 | 77–174 | |





AMTD
6, 6975–7003, 2013



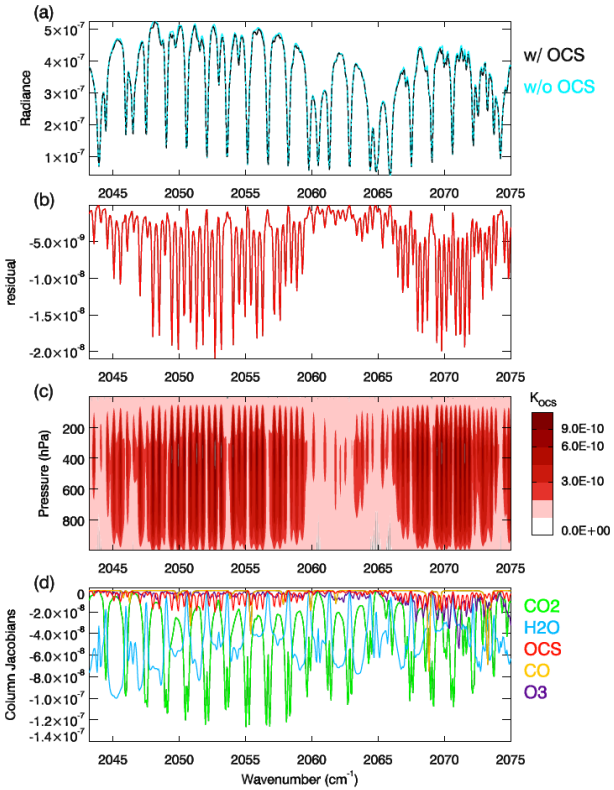


**Fig. 1. (a)** Model calculated radiances without OCS profile (blue line) and with OCS profile (black dash line); **(b)** residuals between the two models calculated radiances in **(a)**; it is the same as OCS column Jacobians, the red line in **(d)**; **(c)** Contour plot for OCS jacobians; **(d)** column Jacobians for $CO_2$ (green), $H_2O$ (blue), OCS (red), CO (orange) and $O_3$ (purple).





AMTD
6, 6975–7003, 2013



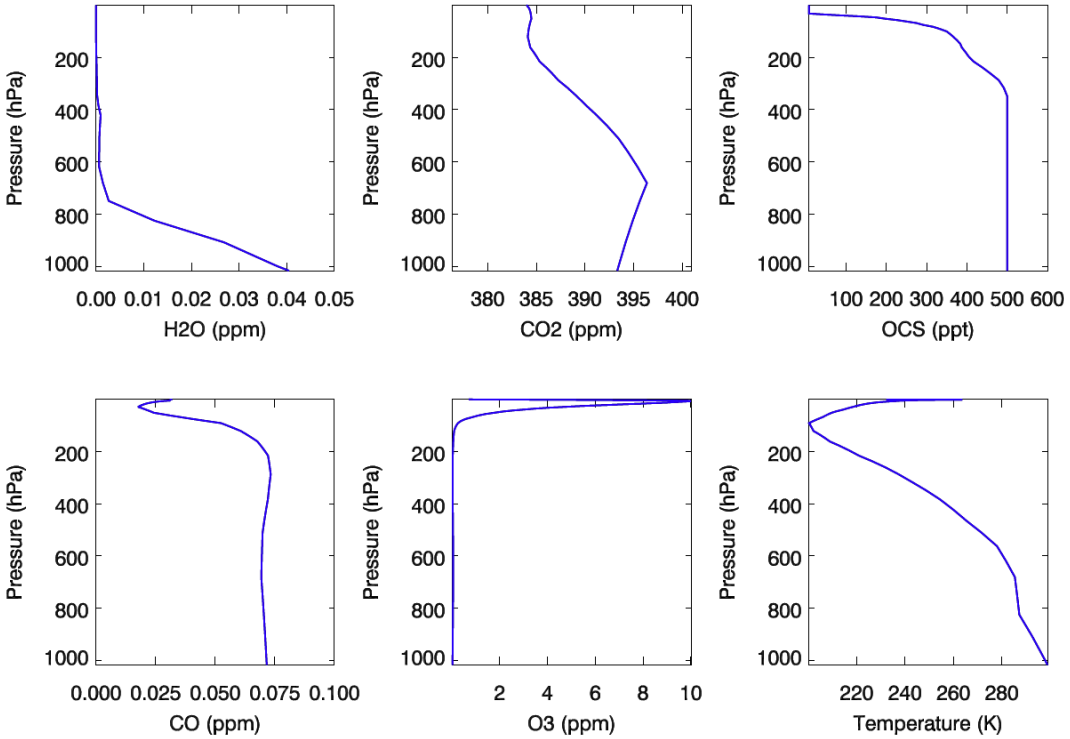


**Fig. 2.** Examples of $H_2O$, $CO_2$, OCS a priori profiles on the top and the state of other variables (e.g. CO, $O_3$, and temperature) on the bottom.





AMTD
6, 6975–7003, 2013



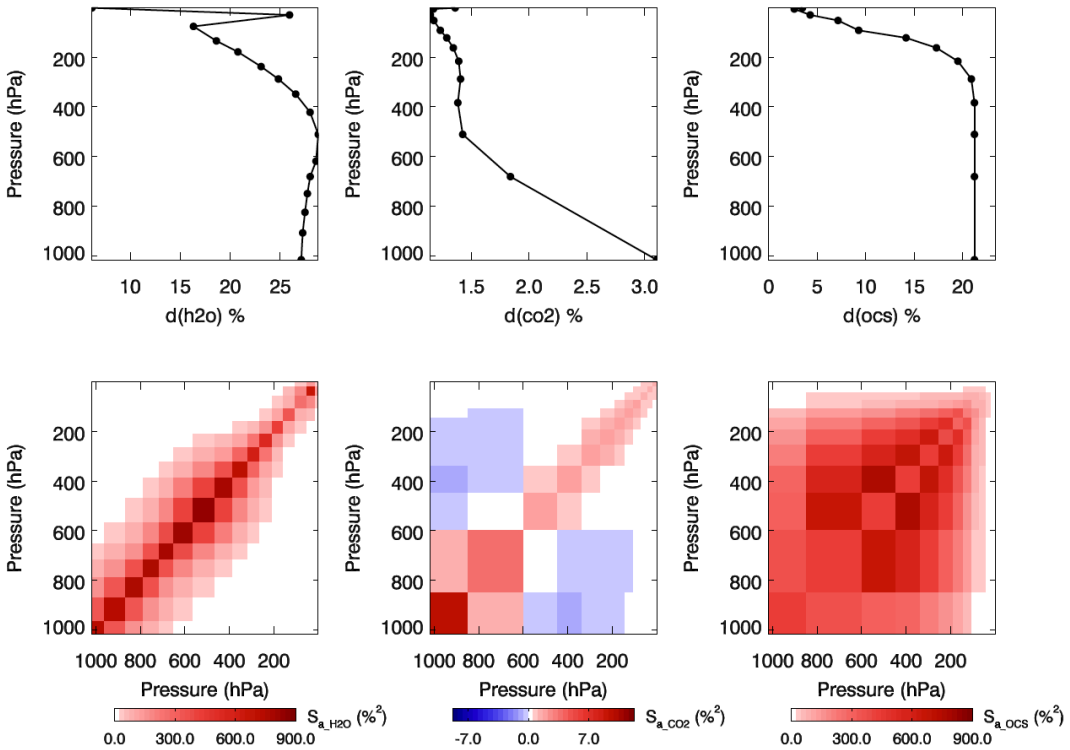


**Fig. 3.** Top row: square root of the diagonal values of the covariance matrices for $H_2O$, $CO_2$ and OCS. Bottom row: corresponding covariance matrices.





AMTD
6, 6975–7003, 2013

Aura tropospheric emissions spectrometer carbonyl sulfide

L. Kuai et al.

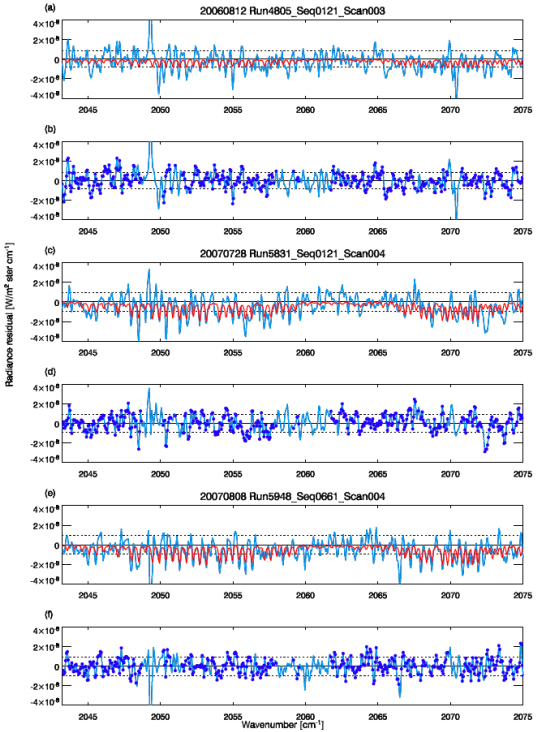


**Fig. 4.** Carbonyl sulfide spectral signal in the TES observations. In **(a)**, **(c)**, and **(e)**, shown in light blue lines without dots (*d*1) are the differences between measured TES spectra and forward-model runs, with retrieved $CO_2$ and $H_2O$ but no OCS; red lines (*d*2) are differences between both forward-model runs with and without OCS or OCS column jacobians. In **(b)**, **(d)**, and **(f)**, shown in light blue with dots (*d*3) are the residuals after OCS retrieval. Dots indicate the frequency of the channels used for retrieval. Solid black lines are the zero lines and dashed lines represent the noise level.





AMTD
6, 6975–7003, 2013



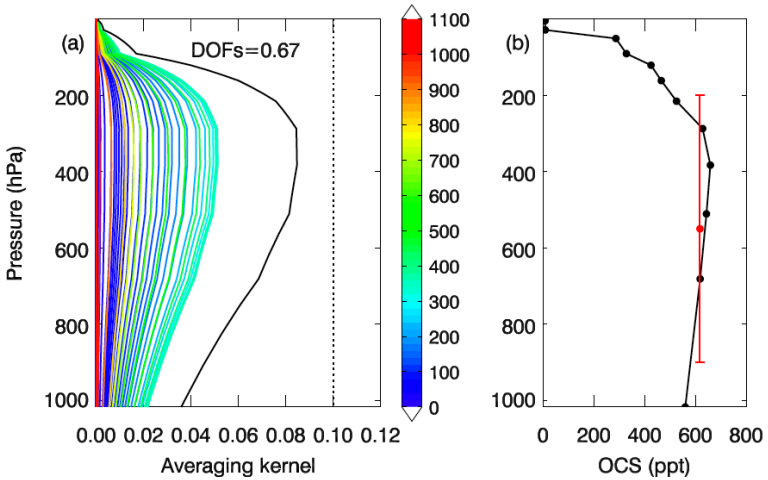


**Fig. 5. (a)** Averaging kernels for different vertical levels in colored lines. The black line represents the one tenth of column averaging kernel. The dotted line is the constant of 0.1 for the reference of column averaging kernel. **(b)** Retrieved OCS profile (black line with dots) and its corresponding tropospheric OCS in red.





AMTD
6, 6975–7003, 2013



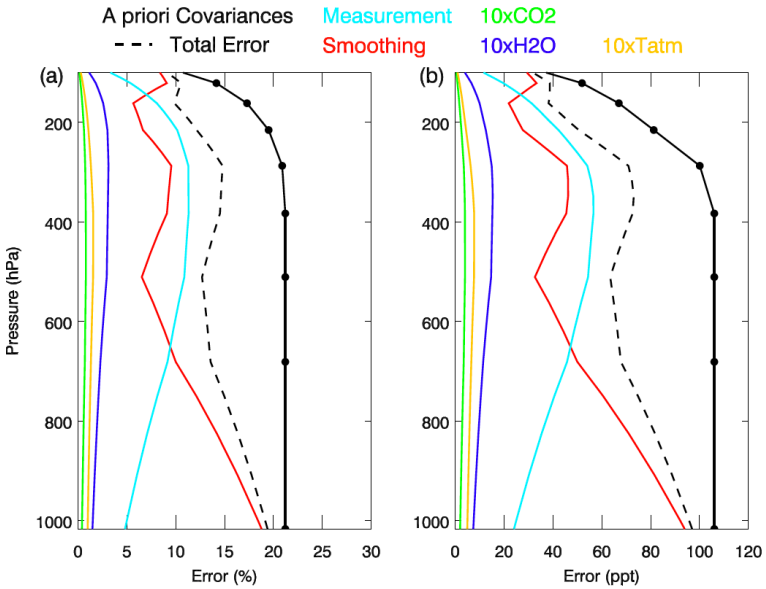


**Fig. 6.** Estimated errors for a single sounding retrieval near Mauna Loa. The non-optimal assumed variability used to constrain the OCS retrieval is the black line with dots. The a posteriori total error (dash line) is composed of smoothing error (red), measurement error (light blue), and systematic errors due to $H_2O$ (dark blue), $CO_2$ (green) and atmospheric temperature (yellow). Note that since the systematic error owing to other trace gases or temperature is quite small compare to other errors, we multiply the errors by ten. **(a)** Errors in percentage. **(b)** Errors in units of ppt.





AMTD
6, 6975–7003, 2013



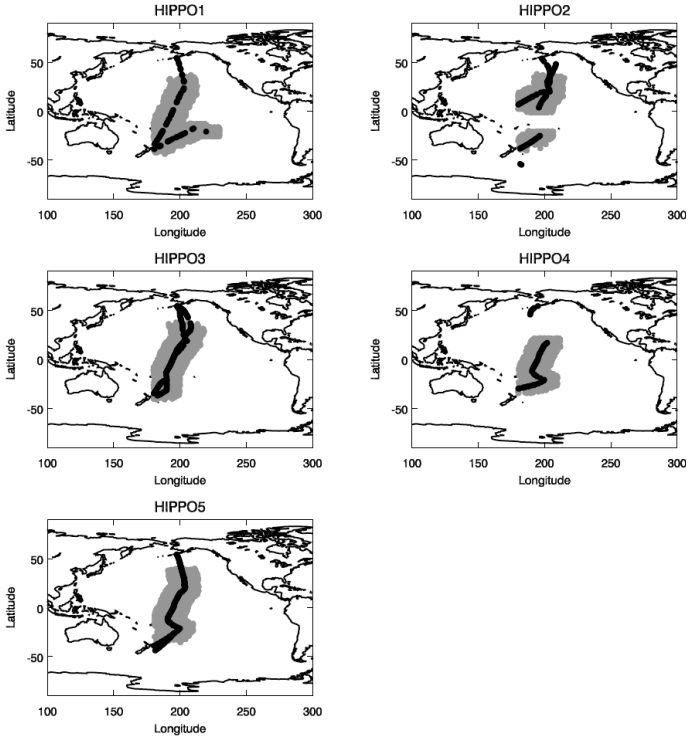


**Fig. 7.** HIPPO campaign trajectory in black dots. The gray region shows the coverage of overpassed TES measurements within the grid box of ±10° about each HIPPO measurement and during the ±15 days period of the years from 2006 to 2010. Both of the HIPPO and TES OCS profiles are vertically averaged between 900 hPa and 200 hPa and latitudinal averaged onto regular grids from 35° S to 35° N every 10°.





AMTD
6, 6975–7003, 2013



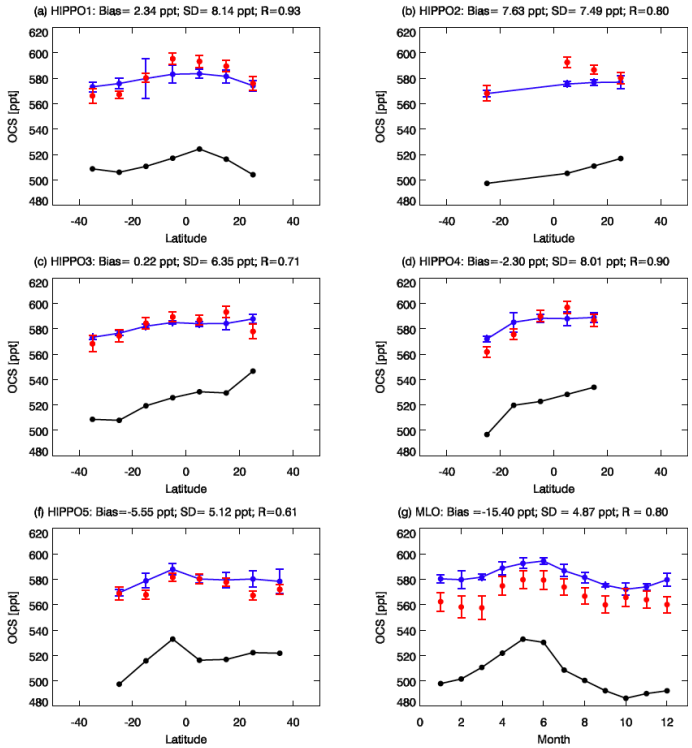


**Fig. 8.** Individual comparison between TES multi-year monthly means and in situ data for latitudinal patterns **(a–f)** and seasonal variations **(g)**. Original in situ data averaged over latitude bins in black; in situ data applied with TES operator in blue; TES data in red. Bias, standard deviation (SD) and correlations ($R$) for the comparison between blue and red are given. Error bar represents the error on the mean (standard variation within the grid bin divided by the square root of the number of observations).





AMTD
6, 6975–7003, 2013



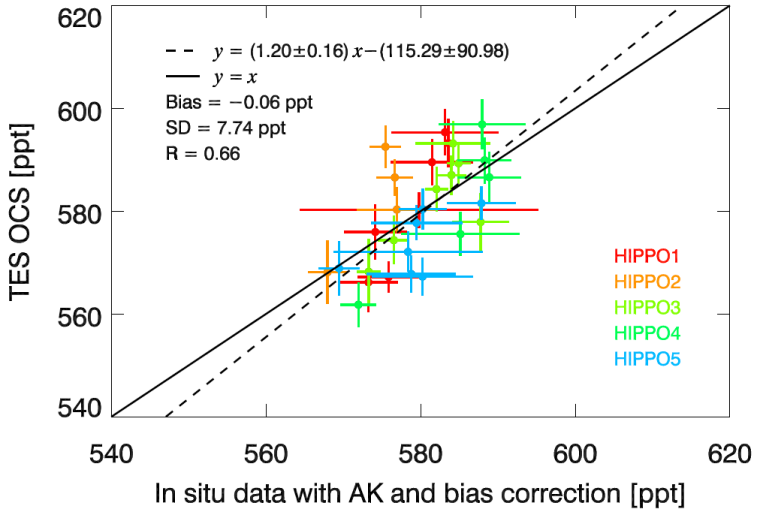


**Fig. 9.** The correlation plot of TES vs. HIPPO in situ data with TES operator. The dashed line shows the linear fit and the solid line is one-to-one line for reference. The bias is close to zero because it has been removed by TES operator. Standard deviation (SD) of the difference is 7.74 ppt and the correlation coefficient ($R$) is 0.66. The color indicates the comparison to each HIPPO campaign. The error bar is the error on the mean.





AMTD
6, 6975–7003, 2013



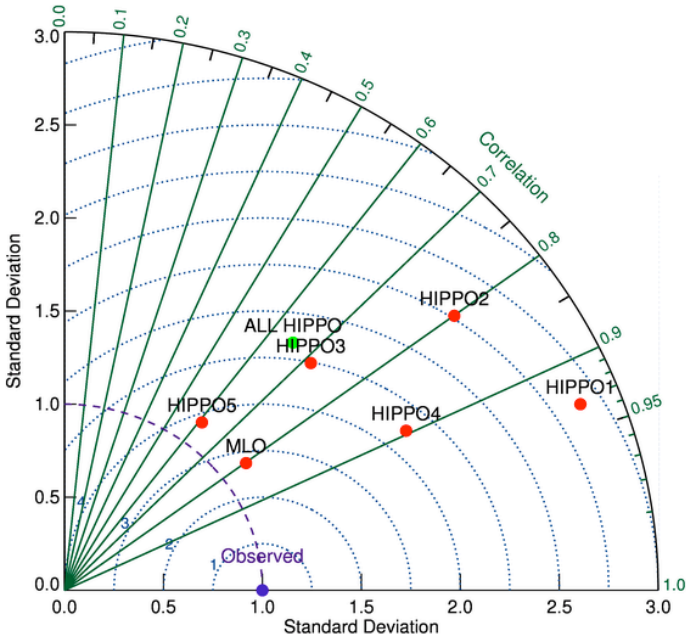


**Fig. 10.** Taylor diagram of TES OCS compared to in situ data.





AMTD
6, 6975–7003, 2013